Beyond Calibration: Assessing the Probabilistic Fit of Neural Regressors via Conditional Congruence

Spencer Young
Delicious AI
spencer.young@deliciousai.com

Cole Edgren
Brigham Young University
coleedgren@gmail.com

Riley Sinema
Brigham Young University
rsinema@student.byu.edu

Andrew Hall
Brigham Young University
amh1124@student.byu.edu

Nathan Dong
Brigham Young University
nathanasaydong@gmail.com

Porter Jenkins
Brigham Young University
pjenkins@cs.byu.edu

Abstract

While significant progress has been made in specifying neural networks capable of representing uncertainty, deep networks still often suffer from overconfidence and misaligned predictive distributions. Existing approaches for addressing this misalignment are primarily developed under the framework of calibration, with common metrics such as Expected Calibration Error (ECE). However, calibration can only provide a strictly marginal assessment of probabilistic alignment. Consequently, calibration metrics such as ECE are *distribution-wise* measures and cannot diagnose the *point-wise* reliability of individual inputs, which is important for real-world decision-making. We propose a stronger condition, which we term *conditional congruence*, for assessing probabilistic fit. We also introduce a metric, Conditional Congruence Error (CCE), that uses conditional kernel mean embeddings to estimate the distance, at any point, between the learned predictive distribution and the empirical, conditional distribution in a dataset. We show that using CCE to measure congruence 1) accurately quantifies misalignment between distributions when the data generating process is known, 2) effectively scales to real-world, high dimensional image regression tasks, and 3) can be used to gauge model reliability on unseen instances.

1 INTRODUCTION

As more machine learning technologies are deployed into the real world, increasing attention is being paid to the ability of these systems to accurately represent their uncertainty [1]. Faithful uncertainty quantification improves the safety, robustness, and reliability of an ML system in the face of imperfect information about the world [2, 3] and has applications to out-of-distribution detection [4–6], active learning [7, 8], and reinforcement learning [2, 9].

While a variety of methods exist for building uncertainty-aware ML systems, in recent years training neural networks to fit high dimensional probability distributions via maximum likelihood has emerged as an effective strategy [10]. For example, a network trained to minimize cross entropy also maximizes the likelihood of a categorical distribution over the labels. In the regression setting, one can parameterize the mean and variance of a Gaussian distribution [11–13] as the outputs of a neural
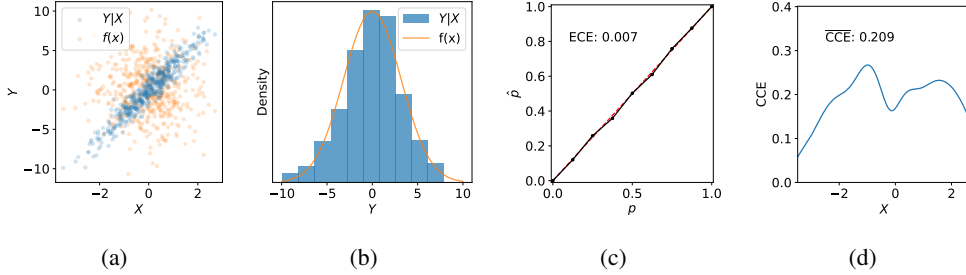
| (a) | (b) | (c) | (d) |

Figure 1: An illustration of the shortcomings of using ECE to measure probabilistic fit in regression problems. We simulate data with the following data-generating process: $X \sim \mathcal{N}(0, 1)$, $Y|X \sim \mathcal{N}(\alpha X, 1)$, $\alpha = 3$, and introduce a poorly specified model, f, that ignores the conditional relationship between X and Y, but has the same marginal: $f(x) \sim \mathcal{N}(0, 1+\alpha^2)$ (see Appendix A.1 for derivation). (a) We plot samples drawn from the true data-generating distribution, $Y|X$, along with samples from the model f; clearly f is misspecified. (b) We marginalize out X from $Y|X$ and plot the histogram of the marginal of Y, next to the PDF of the model, f, showing their statistical equivalence. (c) We compute ECE and plot the associated "reliability" diagram, achieving near-perfect calibration under ECE. (d) Only an input-aware measure of *congruence*, like CCE, correctly recovers the discrepancy between our model and ground-truth distributions and assesses probabilistic fit at each x_i.

network, $\left[\hat{\mu}_i, \hat{\sigma}_i^2\right]^T = \mathbf{f}_{\Theta}(\mathbf{x}_i)$ and maximize the likelihood of the regression targets. When modeling discrete outputs, a similar approach can be employed using a Poisson [14], Negative Binomial [15], or Double Poisson [16] distribution. While these models generally achieve good mean accuracy, they have been shown to produce misaligned predictive distributions and in many cases exhibit overconfident behavior [17, 18].

Such probabilistic misalignment is frequently studied through the framework of *calibration*, which broadly means when a model assigns a probability p to a certain event, in the long run, that event should occur $p\%$ of the time. Historically, the notion of calibration was studied in the context of classification [19], and formalized under the Expected Calibration Error (ECE) metric [20, 21]. More recently, [22] propose an ECE analog for regression problems where empirical quantiles of test data are compared to a model's predicted CDF. Regression-based calibration has received less attention than classification, despite having many relevant applications such as crowd counting [23, 24], traffic flow estimation [25–27], agricultural yield prediction [28], inventory management [29], and cellular bacterial prediction [30]

While ECE is widely used to measure calibration, it has significant shortcomings. Fundamentally, it is a distribution-wise measure, which reduces calibration to a single, aggregated statistic over an entire dataset. In doing so, it can only provide a diagnostic on the *marginal* distribution of the regression targets, P_Y, and is unable to measure the alignment of the *conditional* distribution, $P_{Y|X}$. In fact, a regressor that ignores the input and predicts the marginal distribution of the targets for every instance will be considered calibrated under the paradigm introduced by [22]. See Figure 1 for an example. Moreover, this aggregation sacrifices meaningful signal at the level of each instance; it is unable to assess how well a model communicates uncertainty about a single prediction, $f(x_i)$. Previous work has pointed out "being able to assess the reliability of a probability score for each instance is much more powerful than assigning an aggregate reliability score" [31]. Consider for example, when machine learning is applied to healthcare domains; a patient is likely much more interested in a model's reliability for her specific case than the average reliability of the system across a test dataset [32].

To address these issues, we propose to measure the probabilistic fit of machine learning regression models with a stronger, quantifiable condition, called *congruence*. In contrast to calibration, which is an aggregated, distribution-wise measure of the marginal P_Y, congruence assesses the point-wise uncertainty of the conditional distribution at each specific point, $P_{Y|X=x_i}$. To measure congruence, we propose a novel metric called Conditional Congruence Error (CCE). Rather than rely on quantile- or coverage-based measurements, we leverage recent theoretical advances in conditional kernel mean embeddings [33] to compute conditional congruence by estimating the discrepancy between a model's learned, predictive distribution and the empirical, conditional distribution in a dataset. Our approach does not require distributional assumptions about the data or the evaluation of a likelihood.

We show that using CCE to measure point-wise congruence 1) recovers the true discrepancy between the predictive and ground truth distributions when the data generating process is known, 2) scales to high dimensional problems, such as image regression, and 3) can be used to assess the uncertainty of unseen instances.

2 PRELIMINARIES

2.1 Notation

Suppose we are given an unknown data-generating distribution (X, Y), where Y has a conditional relationship with X, $Y|X$. Let X take values $x \in \mathcal{X}$ and let Y take values $y \in \mathcal{Y}$. We denote $\mathcal{P_Y}$ to be the space of all possible distributions over $\mathcal{Y}$. Let $P_{Y|X} : \mathcal{X} \to \mathcal{P_Y}$ be nature's mapping implied by (X, Y) that takes conditioning values in $\mathcal{X}$ and outputs distributions over $\mathcal{Y}$. By $P_{Y|X=x} \in \mathcal{P_Y}$, we refer to the specific, conditional distribution obtained over $\mathcal{Y}$ given a realization of X, $x \in \mathcal{X}$. P_X and P_Y denote the marginal distributions of X and Y. We assume access to a probabilistic model $f : \mathcal{X} \to \mathcal{P_Y}$, as well as a set $\mathcal{S}$ of n draws from (X, Y), $(x_i, y_i)_{i=1}^n$, that have been withheld from model training.

2.2 Assessing Probabilistic Fit

As discussed above, calibration is not a sufficient condition for a well-fit probabilistic model. Rather than use calibration to evaluate a model, we propose a point-wise condition that more fully captures the desiderata of supervised learning — a model that closely approximates (or is congruent with) the true conditional distribution for any input-output pair:

Definition 1. *A conditional distribution $f(x)$ output by a probabilistic model $f : \mathcal{X} \to \mathcal{P_Y}$ is* congruent *with the true, data-generating distribution (X, Y) if $P_{Y|X=x} = f(x)$. A model f is* conditionally congruent *(otherwise called* point-wise congruent*) if, for all $x \in \mathcal{X}$, $f(x)$ is congruent.*

Quantifying conditional congruence is straightforward — for all $x \in \mathcal{X}$, we compute the distance between the model's learned conditional distribution $f(x)$ and the ground-truth $P_{Y|X=x}$. Adopting the terminology of [34] (which proposes a distance-based definition of marginal calibration in the binary classification setting), given a model f, we quantify its "distance from conditional congruence" (D_C) as follows:

$$D_C(f, P_{Y|X}) = \mathbb{E}_{x \in \mathcal{X}} \big[\rho(f(x), P_{Y|X=x}) \big] \tag{1}$$

where $\rho : \mathcal{P_Y} \times \mathcal{P_Y} \to \mathbb{R}$ measures distance between two probability distributions over $\mathcal{Y}$. Clearly, $D_C(f, P_{Y|X}) = 0$ if and only if f is conditionally, or point-wise, congruent.

3 MEASURING CONDITIONAL CONGRUENCE

Despite the usefulness of Equation 1 for theoretically treating congruence, in practice, an exact calculation of this distance is intractable due to finite data. In this section, we introduce a sample-based method for estimating the point-wise congruence of a model via conditional kernel mean embeddings.

3.1 Maximum Conditional Mean Discrepancy (MCMD)

In machine learning problems that model with uncertainty, we are only given a finite number of draws from (X, Y) to evaluate the quality of a predictive distribution. This introduces great difficulty in estimating $D_C(f, P_{Y|X})$, because we require multiple examples with the exact same conditioning input x to approximate $P_{Y|X=x}$ with any degree of confidence [34]. In most domains, the probability of this occurrence across multiple inputs is essentially zero.

One reasonable assumption to make estimation of $P_{Y|X=x}$ more tractable is that similar inputs should yield similar conditional distributions. Thus, $P_{Y|X=x}$ can be approximated by aggregating (x, y) samples with similar x values. This process is formalized using kernel functions. When a

kernel, $k : \mathcal{X} \times \mathcal{X} \to \mathbb{R}$, is symmetric, continuous, and positive semi-definite, $k(\mathbf{x}, \mathbf{x}')$ represents an inner product $\langle \phi(\mathbf{x}), \phi(\mathbf{x}') \rangle_{\mathcal{V}}$ in some (possibly higher-dimensional) feature space $\mathcal{V}$, thus yielding a similarity measure in that space.

Kernel mean embeddings [35] extend the idea of applying a higher-dimensional feature map, ϕ, to the space of probability distributions, $\mathcal{P}_X$. Let $P \in \mathcal{P}_{\mathcal{X}}$ be a probability distribution over $\mathcal{X}$. Then the kernel mean embedding is defined as $\phi(P) = \mathcal{U}_P \triangleq \int_{\mathcal{X}} k(\mathbf{x}, \cdot) dP(\mathbf{x})$. In this formulation, P is represented as $\mathcal{U}_P \in \mathcal{H}$, an element of an infinite-dimensional reproducing kernel Hilbert space (RKHS) [35]. One application of this technique is the maximum mean discrepancy (MMD), which estimates the distance between two distributions, $P \in \mathcal{P}_{\mathcal{X}}$ and $Q \in \mathcal{P}_{\mathcal{X}}$, by computing the magnitude of the difference between their respective mean embeddings: $\text{MMD}(P, Q) = \|\mathcal{U}_P - \mathcal{U}_Q\|_{\mathcal{H}}$. Using the kernel trick we can estimate this distance (which is an inner product) from data points without having to explicitly evaluate the mapping $\phi(x)$.

The MMD was extended to the conditional probability setting by [35], resulting in the Maximum Conditional Mean Discrepancy (MCMD). Let $P_{Y|X}$ and $P_{Y'|X'}$ be two mappings from $\mathcal{X}$ to $\mathcal{P}_{\mathcal{Y}}$ implied by the (possibly equivalent) joint distributions (X, Y) and (X', Y'). Then, given conditional kernel mean embeddings (defined for each $x \in \mathcal{X}$), we have $\text{MCMD}(P_{Y|X}, P_{Y'|X'}, \cdot) = \|\mathcal{U}_{Y|X}(\cdot) - \mathcal{U}_{Y'|X'}(\cdot)\|_{\mathcal{H}_{\mathcal{Y}}}$. Recently, [33] derived a closed-form estimate of MCMD, which we provide in Equation 2.

3.1.1 Computing MCMD

Given a set of draws $\mathcal{S} = (x_i, y_i)_{i=1}^n \sim (X, Y)$ and $\mathcal{S}' = (x_i', y_i')_{i=1}^m \sim (X', Y')$, we have the following closed-form, sample-based estimate from [33] for the squared MCMD at a given conditioning value $(\cdot) \in \mathcal{X}$:

$$
\begin{aligned}
\widehat{\text{MCMD}}^2(\mathcal{S}, \mathcal{S}', \cdot) = {}& \mathbf{k}_X^T(\cdot) \mathbf{W}_X \mathbf{K}_Y \mathbf{W}_X^T \mathbf{k}_X(\cdot) \\
& - 2\mathbf{k}_X^T(\cdot) \mathbf{W}_X \mathbf{K}_{YY'} \mathbf{W}_{X'}^T \mathbf{k}_{X'}(\cdot) \\
& + \mathbf{k}_{X'}^T(\cdot) \mathbf{W}_{X'} \mathbf{K}_{Y'} \mathbf{W}_{X'}^T \mathbf{k}_{X'}(\cdot)
\end{aligned}
\tag{2}
$$

where we first choose input and output kernels $k_{\mathcal{X}}$ and $k_{\mathcal{Y}}$, yielding $\mathbf{K}_Y^{(ij)} = k_{\mathcal{Y}}(y_i, y_j)$, $\mathbf{K}_{Y'}^{(ij)} = k_{\mathcal{Y}}(y_i', y_j')$, $\mathbf{K}_{YY'}^{(ij)} = k_{\mathcal{Y}}(y_i, y_j')$, $\mathbf{K}_X^{(ij)} = k_{\mathcal{X}}(x_i, x_j)$, $\mathbf{K}_{X'}^{(ij)} = k_{\mathcal{X}}(x_i', x_j')$, $\mathbf{k}_X(\cdot) = [k_{\mathcal{X}}(x_1, \cdot), ..., k_{\mathcal{X}}(x_m, \cdot)]^T$, $\mathbf{k}_{X'}(\cdot) = [k_{\mathcal{X}}(x_1', \cdot), ..., k_{\mathcal{X}}(x_m', \cdot)]^T$, $\mathbf{W}_X = (\mathbf{K}_X + n\lambda \mathbf{I}_n)^{-1}$ and $\mathbf{W}_{X'} = (\mathbf{K}_{X'} + m\lambda' \mathbf{I}_m)^{-1}$

Both λ and λ' are regularizing hyperparameters that we set to 0.1 throughout this paper. We study the effect of λ in Appendix C.3.

3.1.2 Theoretical Guarantees of MCMD

[33] provide a handful of theoretical guarantees associated with the MCMD. The most relevant to our work (Theorem 5.2 in the original paper) is restated below, with adjustments to match our notation:

Theorem 1. *Suppose $k_{\mathcal{X}}$ and $k_{\mathcal{Y}}$ are characteristic kernels. Also suppose that the probability measures associated with X and X' in the conditioning space, P_X and P_X', are absolutely continuous with respect to each other. Finally, suppose that $P_{Y|X}$ and $P_{Y'|X'}$ admit regular versions. Then $MCMD(P_{Y|X}, P_{Y'|X'}, \cdot) = 0$ almost everywhere if and only if the set of conditioning inputs $\{x \mid x \in \mathcal{X}, \exists\, y \in \mathcal{Y} \text{ s.t. } P_{Y|X=x}(y) \neq P_{Y'|X'=x}(y)\}$ has probability zero.*

This is a useful theorem, and as stated by [33], does not have restrictive assumptions. We note that the guarantees are given in terms of $\text{MCMD}(P_{Y|X}, P_{Y'|X'}, \cdot)$ and not the estimate $\widehat{\text{MCMD}}^2$. However, if we also assume bounded kernels (once again, not restrictive), [33] provide several desirable convergence properties with their estimate (see Theorems 4.4, 4.5 in their paper) that give us confidence in employing the MCMD as a measure of congruence.

If a model f yields samples that achieve near-zero MCMD when compared to the ground-truth samples, these theoretical results ensure that the model has learned a conditional probability distribution with an almost-sure equality to the ground-truth data-generating distribution. In fact, this allows us to use the MCMD to directly estimate $D_C(f, P_{Y|X})$, as detailed in the next section.
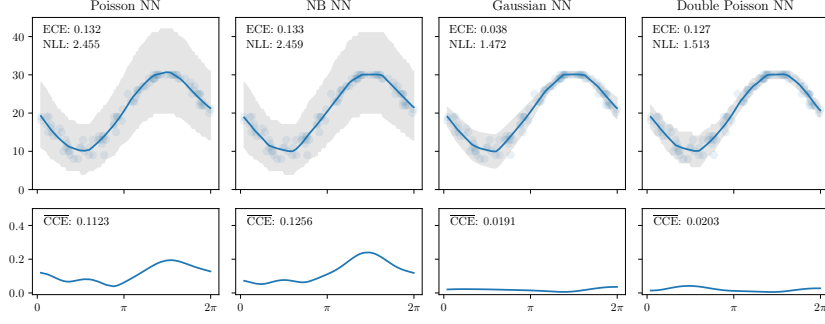
Figure 2: Visualization of the probabilistic fit of 4 deep neural networks on a synthetic dataset with discrete regression targets. (Row 1) A plot of the mean and centered 95% credible interval for each model, along with the ECE and NLL. (Row 2) CCE between the ground-truth and predictive distributions, along with the mean value ($\overline{\text{CCE}}$) across the evaluation grid.

3.2 Conditional Congruence Error

While the MCMD is a powerful theoretical tool, applying it to high-dimensional joint distributions common to deep learning introduces two main challenges: 1) representation of the inputs in a space that lends itself to kernelized similarities; and 2) a method for defining (and obtaining samples from) (X', Y') given only a test set $S = (x_i, y_i)_{i=1}^n$ and a model f. We specify a process that addresses both challenges, thus yielding a metric, the Conditional Congruence Error (CCE), that provides a holistic look at a model's probabilistic fit across the input space.

To compute the CCE, we first specify an encoding function $\varphi : \mathcal{X} \to \mathbb{R}^d$ that can map each complex input (images, text, etc.) to a fixed-length vector in a semantic embedding space, similar to [36] and [37]. We then embed each input in our test set and treat $\mathcal{S}_\varphi = (\varphi(x_i), y_i)_{i=1}^n$ as our sample from nature's distribution $(\varphi(X), Y)$. To obtain $\mathcal{S}'_\varphi = (\varphi(x'_i), y'_i)_{i=1}^m \sim (\varphi(X'), Y')$, we draw ℓ Monte Carlo samples from each predictive distribution $f(x_i)$. This forms a collection of $m = n\ell$ draws $\{(\varphi(x_i), y_{ik})_{k=1}^\ell\}_{i=1}^n$ from the model's learned conditional distributions which we can then compare with the ground-truth draws. Armed with these samples, we can now define CCE:

$$\text{CCE}(f, \mathcal{S}, \varphi, \cdot) = \sqrt{\widehat{\text{MCMD}}^2(\mathcal{S}_\varphi, \mathcal{S}'_\varphi, \cdot)} \qquad (3)$$

Unless otherwise specified, we use CLIP [38] as our choice of φ due to its impressive representational capacity and ease of implementation using libraries such as OpenCLIP [39]. For $k_\mathcal{X}$, we use the polynomial kernel, $k(\mathbf{x}, \mathbf{x}') = (\frac{1}{d}\mathbf{x}^T\mathbf{x}' + 1)^3$, similar to [40]. When forming $\mathcal{S}'_\varphi$, we draw $\ell = 1$ samples per test point. For $k_\mathcal{Y}$, we use the radial basis function (RBF) kernel $k(\mathbf{x}, \mathbf{x}') = \exp{-\gamma \|\mathbf{x} - \mathbf{x}'\|^2}$, with $\gamma = \frac{1}{2\hat{\sigma}_y^2}$, where $\hat{\sigma}_y^2 = \frac{1}{n-1}\sum_{i=1}^n(y_i - \bar{y})^2$ is estimated from our test targets. Empirically, we find that this choice of kernels and hyperparameters yields well-behaved CCE values that match with intuition. For a more extensive investigation of hyperparameters, see Appendix C.3.

Once we fix $\mathcal{S}$, the CCE is defined for any input $x \in \mathcal{X}$, even if we do not have an associated label $y \in \mathcal{Y}$. This makes it a powerful tool for quantifying model reliability in a variety of deployment settings where labels are not known. We show how this property enables point-wise diagnostics in Section 4.3, and demonstrate how it yields a natural algorithm for the subfield of machine learning with rejection in Appendix C.1.

To evaluate a model's congruence, we compute the CCE for each x_i in our test data. The resultant array of values provides a notion of probabilistic alignment across the entire input space. When a single summary statistic is desired, we take the mean of these CCE values (denoted $\overline{\text{CCE}}$). An algorithm describing our process in greater detail can be found in Appendix B.1.

Note that since $\mathcal{U}_{Y|X}(x)$ can be considered a representation of $P_{Y|X=x}$, with $\mathcal{U}_{Y'|X'}(x)$ a representation of $f(x)$ (in an infinite-dimensional Hilbert space), if we let ρ be the distance metric induced by $\|\cdot\|_{\mathcal{H}_Y}$, $\overline{\text{CCE}}$ can be viewed as a direct estimate of $D_C(f, P_{Y|X})$ as defined in Equation 1.
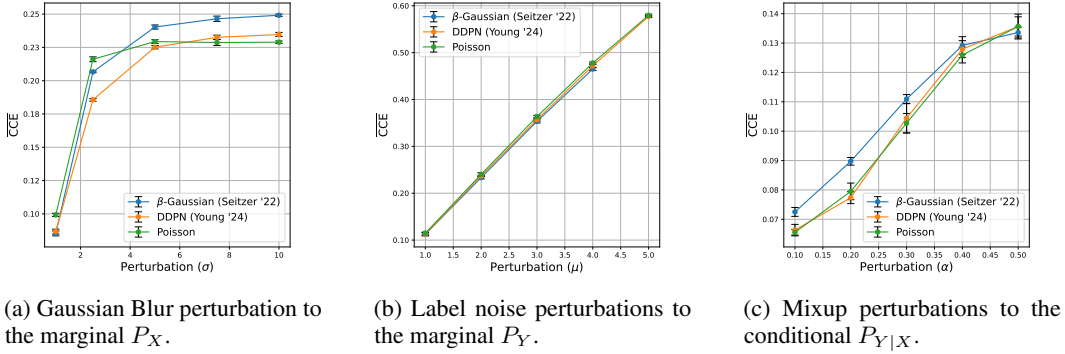
5

(a) Gaussian Blur perturbation to the marginal P_X.

(b) Label noise perturbations to the marginal P_Y.

(c) Mixup perturbations to the conditional $P_{Y|X}$.

Figure 3: We train three neural regression models (Poisson, β-Gaussian [41], and DDPN [16]) on the count regression task of `COCO-People` and apply progressively increasing levels of perturbation to the test data. We assess the ability of CCE to describe the misalignment of each model's predictive distribution. (a) We increase the level of Gaussian blur (σ) to the pixels of each image, thus modifying P_X; (b) we apply Gaussian noise with constant variance ($\mu, \sigma = 1.0$) to each label, modifying P_Y; (c) We apply the Mixup augmentation [42], $(1 - \alpha)z_1 + \alpha z_2$, to both the images and labels and perturb the conditional, $P_{Y|X}$. Under all three perturbation regimes, we see that CCE is effective at describing increasing levels of incongruence between the model's predictive distribution and the test data. This effect is invariant to the choice of model.

4 EXPERIMENTS

To demonstrate the effectiveness of CCE, we show how it can both quantify a model's overall probabilistic fit and act as a point-wise diagnostic tool for identifying specific model shortcomings. First, we show how CCE effectively recovers the true discrepancy between a predictive distribution and test data when the data generating process is known. Second, we show how CCE scales to high-dimensional image regression tasks, and again effectively identifies distributional misalignment under known perturbations to the data. Third, we show how CCE compares to existing measures of probabilistic fit across a variety of image regression tasks. Finally, we include two case studies in which we use the CCE to pinpoint areas in the input space where models are most- and least-congruent. All code used in these experiments is freely available online[1].

In our experiments, CCE is compared to ECE, which directly measures calibration, and Negative Log Likelihood (NLL), which is a proper scoring rule [43]. In contrast to ECE, NLL can be evaluated point-wise, but requires distributional assumptions, is difficult to compare across regressors, and is sensitive to outliers. In Appendix D.2 we show that point-wise NLL is subject to these pathologies and that CCE avoids them. Finally, in Appendix C.3 we perform extensive hyperparameter studies for λ, γ, ℓ and the choice of kernel.

4.1 CCE with a Known Data-Generating Process (Synthetic Data)

Our primary aim is to demonstrate that CCE can effectively evaluate a model's overall probabilistic fit. We first use a synthetic dataset [16]) where the true data-generating process is known. The data describe a one-dimensional discrete synthetic regression problem that exhibits various levels of dispersion, with high levels of uncertainty at low counts and severe under-dispersion at high counts. Both continuous and discrete neural regressors can be fit to this dataset. We train a small multi-layer perceptron (MLP) to output the parameters of a `Poisson`, `Negative Binomial` (NB), `Gaussian`, and `Double Poisson` distribution [16] using the appropriate NLL loss. The models' predictive distributions over the test split of the dataset are visualized in row 1 of Figure 2, with the respective NLL and ECE of the model overlaid on the plot. We also compute the CCE for each model on all test inputs. We plot the resultant values in row 2 of Figure 2 (with $\overline{\text{CCE}}$ indicated in each respective plot). Since our inputs, x_i, are one-dimensional, we set φ to be the identity and use the RBF kernel with $\gamma = 0.5$ for $k_{\mathcal{X}}$.

---
[1] `https://anonymous.4open.science/r/probcal-8294`

The `Poisson` and `Negative Binomial` distributions do not have the flexibility to represent under-dispersion. Accordingly, they struggle most in the $[\pi, 2\pi]$ region of the input (where the requisite regression targets have very low variance). This is where the CCE identifies the largest incongruence between the model and the data. Meanwhile, the `Gaussian` and `Double Poisson` models achieve much more aligned predictive distributions. This is supported by their near-zero CCE values. Measuring congruence via CCE allows us to (rightly) conclude that the `Gaussian NN` and `Double Poisson NN` achieve the best probabilistic fit.

In Figure 2 we observe disagreement between the CCE and ECE when assessing the probabilistic fit of the `Gaussian` and `Double Poisson` models. In fact, as further expanded upon in Appendix D.1, this may be due to an implicit bias in the ECE computation against discrete models. We also note that though the NLL suggests a similar ranking of models as the CCE in this scenario, its undetermined lower bound makes it difficult to quantify how close to perfectly fit each model is, since the NLL cannot be easily interpreted as an estimate of $D_C(f, P_{Y|X})$.

Table 1: Comparison of ECE, NLL, and $\overline{\text{CCE}}$. We denote the best performer on each metric in **bold** and the second-best performer with an underline.

	COCO-People			FG-Net			AAF		
	ECE ($\downarrow$)	NLL ($\downarrow$)	$\overline{\text{CCE}}$ ($\downarrow$)	ECE ($\downarrow$)	NLL ($\downarrow$)	$\overline{\text{CCE}}$ ($\downarrow$)	ECE ($\downarrow$)	NLL ($\downarrow$)	$\overline{\text{CCE}}$ ($\downarrow$)
Poisson NN	0.088	2.316	**0.061** (0.001)	0.039	<u>3.027</u>	0.062 (0.011)	0.035	**3.324**	<u>0.026</u> (0.003)
NB NN	0.067	**2.248**	<u>0.072</u> (0.002)	**0.023**	**2.863**	**0.043** (0.014)	**0.023**	<u>3.380</u>	**0.022** (0.003)
DDPN	**0.052**	<u>2.270</u>	0.075 (0.001)	0.054	3.300	0.082 (0.010)	0.091	3.433	0.051 (0.004)
Gaussian NN	0.078	2.411	0.125 (0.001)	0.050	3.144	<u>0.049</u> (0.001)	<u>0.027</u>	3.432	<u>0.026</u> (0.003)
Stirn et al. [12]	0.081	2.650	0.140 (0.002)	<u>0.031</u>	3.142	0.065 (0.019)	0.104	4.230	0.042 (0.002)
Immer et al. [13]	0.057	2.298	0.081 (0.001)	0.626	10.843	0.657 (0.001)	0.026	3.430	0.031 (0.003)
Seitzer et al. [41]	<u>0.055</u>	2.374	<u>0.072</u> (0.002)	0.093	3.618	0.079 (0.003)	0.115	4.252	0.063 (0.001)

Table 2: Comparison of ECE, NLL, and $\overline{\text{CCE}}$ for the EVA dataset (a continuous image regression task). We denote the best performer on each metric in **bold** and the second-best performer with an underline.

	EVA		
	ECE ($\downarrow$)	NLL ($\downarrow$)	$\overline{\text{CCE}}$ ($\downarrow$)
Gaussian NN	0.235	1.563	0.086 (0.009)
Stirn et al. [12]	**0.148**	1.404	0.100 (0.007)
Immer et al. [13]	<u>0.165</u>	**1.207**	**0.041** (0.002)
Seitzer et al. [41]	0.194	<u>1.389</u>	<u>0.068</u> (0.004)

4.2 CCE with an Unknown Data-Generating Process (Image Regression)

In the following section we demonstrate that CCE can effectively scale beyond low-dimensional data. To do so, we perform a series of image regression tasks. In real-world problems, the data generating process is not known. However, we show that CCE is effective at identifying increasing divergence between a model's predictive distribution and test data when we apply growing levels of perturbations. We then provide a comparison of CCE, ECE, and NLL across a variety of datasets.

4.2.1 CCE Under Known Distribution Shift

We perform an image regression task where the goal is to accurately predict the number of people in an image using the 'person' class of the MS-COCO dataset [44]. The bounding boxes for each image have been translated into a single, discrete count [16]. This task allows us to train regressors with both continuous and discrete predictive distributions.

We train three different regression models, each with a different predictive distribution: a Poisson NN [14], β-Gaussian ($\beta = 0.5$) [41] and DDPN [16]. Each network is trained with the same backbone, the pooled output from a ViT [45] (initialized from the `vit-base-patch16-224-in21k` checkpoint). Both β-Gaussian and DDPN are modern, highly flexible regressors, while Poisson is subject to equi-dispersion and has a more rigid parametric form. This diversity in models allows us to observe how well CCE captures increasing levels of data shift under a variety of predictive distributions.

For each model, we perform three types of data shift. First, we apply varying levels of Gaussian blur to the input image, which perturbs the marginal of the input, P_X, away from the training data. Second, we apply Gaussian noise to the marginal of the output, P_Y. Third, we apply the Mixup transform [42] to both the images and the labels, which is a perturbation to the conditional, $P_{Y|X}$. For each model, we perform five trials of the data perturbation strategy and evaluation, and plot the mean and standard deviation of the resulting $\overline{\text{CCE}}$ statistic. For each instance in the test data, we draw a single Monte Carlo sample from the predictive distribution ($\ell = 1$).

Results are shown in Figure 3. We see that under all three data shift regimes, $\overline{\text{CCE}}$ smoothly increases as as perturbations of progressively larger magnitude are applied. Additionally, we observe that because CCE is a measure of conditional congruence, it can identify misalignment in both the conditional, $P_{Y|X}$, and marginal distributions, P_X and P_Y. Additionally, CCE can even detect divergence when a model's predictive distribution is less expressive, such as the Poisson network, which only has one parameter to represent predictive mean and variance.

4.2.2 Comparing CCE to ECE and NLL Across Datasets

Next we diagnose the behavior of CCE across a variety of tasks and datasets. In these experiments, there is no model that is a priori known to be best-fit, and the data generating process is unknown. Our goal is to compare and contrast the measures of probabilistic alignment provided by $\overline{\text{CCE}}$, ECE, and NLL.

The regression tasks studied include the `COCO-People` task introduced above, predicting a person's age from an image (`FG-Net` [46], `AAF` [47]), and regressing a score describing how appealing an image is (`EVA` [48]). On all counting tasks (`COCO-People`, `FG-Net`, and `AAF`), we train a Poisson NN [14], a Negative Binomial NN [15], a DDPN [16], a vanilla Gaussian NN [2] [11], and modern Gaussian regressors such the β-modified Gaussian ($\beta = 0.5$) [41], the naturally parameterized Gaussian [13], and the "faithful" heteroscedastic regressor [12]. For the `EVA` dataset, we only benchmark Gaussian models since the labels are continuous. All architecture, hardware, and hyperparameter details for these experiments can be found in Appendix A.2.

Tables 1 and 2 contain the $\overline{\text{CCE}}$, ECE and NLL for different models trained on `COCO-People`, `FG-Net`, `AAF`, and `EVA`. We compute $\overline{\text{CCE}}$ 5 times and report the mean and standard deviation of this statistic (in parentheses) across trials. CCE values were computed according to the description in Section 3.2.

In general, we observe broad agreement among $\overline{\text{CCE}}$, ECE, and NLL. The best model with respect to conditional congruence ($\overline{\text{CCE}}$) also exhibits the best (or near-best) marginal calibration (ECE) and average NLL. For example, on `FG-Net`, the Negative Binomial NN achieves the lowest error by all three measures. On `AAF`, Negative Binomial is once again the best performer on ECE and $\overline{\text{CCE}}$. Meanwhile, [13] scores best on NLL and $\overline{\text{CCE}}$ while coming in second with its ECE. These results are to be expected — since point-wise congruence implies marginal calibration, our metrics should tend toward agreement in the aggregate.

4.3 Diagnosing Point-wise Model Failures with CCE

While $\overline{\text{CCE}}$ is an effective overall descriptor of probabilistic fit, one of the greatest virtues of CCE is as a point-wise reliability measure. Specifically, by viewing the inputs that incur both the highest and lowest CCE values, we can gain insight into a model's performance on specific regions of $\mathcal{X}$. Most importantly, this analysis can be done without access to labels. To do this, we take $\mathcal{S}$ to be the *validation* split of a dataset, and evaluate $\text{CCE}(f, \mathcal{S}, \varphi, \cdot)$ at all inputs from the *test* split. The resultant values provide insight into the types of examples the model is best- and worst-fit on. We demonstrate this diagnostic process on two model-dataset pairs: [41]'s β-Gaussian that has been fit on the `AAF` dataset (see Figure 4) and the Poisson NN trained on `COCO-People` (see Figure 5).

In the first row of Figure 4, we plot the images from `AAF` with the lowest CCE values in our test data. These are images where the model's learned conditional distributions are most congruent with the true data-generating distribution. In the second row, we plot the images with the highest CCE values, where the model's distributions are least congruent. According to our measurement, the

---

[2] Although modeling discrete data with a Gaussian distribution is not entirely proper, it is a common practice due to the distribution's flexibility.

model struggles most in terms of probabilistic alignment when predicting the ages of young-adult women, while it appears to be more reliable when given images of middle-aged males, shedding light on possible biases learned by our model. While the `AAF` dataset is made up of around 55% female faces, each model's feature extractor was pre-trained on much larger datasets where racial or gender bias likely exists [49].

Figure 5 reveals where the Poisson NN trained on `COCO-People` performs best (top row) and worst (bottom row) with respect to CCE. Interestingly, the Poisson model struggles to form distributions over severely high counts in crowded scenes. This may be due to the rigid equivariance assumption inherent to a Poisson model. If the true data-generating distribution in the region of "large crowds" is under- or over-dispersed, the Poisson NN would not be able to represent this fact. Thus, the model outputs distributions over $\mathcal{Y}$ that are incongruent with the ground truth. Overall, this analysis provides an effective framework for discovering point-wise incongruence for test examples.

Figure 4: Test images that incurred the lowest (first row) and highest (second row) CCE values for a β-Gaussian model [41] trained on the AAF dataset. CCE values indicated above each image. High values correspond to the largest distance between learned and actual conditional distributions.

Figure 5: Lowest and highest CCE values for a Poisson NN trained on `COCO-People`.

5 Conclusion

In this paper, we identify issues with current approaches used to evaluate the quality of predictive distributions produced by neural networks. We show that existing measurements that target calibration are inherently marginal and ignore conditional dependencies in the data. To address this, we introduce a stronger definition of probabilistic fit, called congruence, and propose Conditional Congruence Error (CCE) as a novel measure. CCE is a conditional, rather than marginal, statistic and can be computed point-wise for unseen test instances. We show CCE can effectively recover divergence between predictive distributions and test data and can be used to interpret failure cases of a model. Future work should study open questions about using CCE in the classification setting, using CCE as a regularizer during training, or incorporating point-wise CCE values into an active learning framework.

References

[1] M. Abdar, F. Pourpanah, S. Hussain, D. Rezazadegan, L. Liu, M. Ghavamzadeh, P. Fieguth, X. Cao, A. Khosravi, U. R. Acharya *et al.*, "A review of uncertainty quantification in deep learning: Techniques, applications and challenges," *Information fusion*, vol. 76, pp. 243–297, 2021.

[2] T. Yu, G. Thomas, L. Yu, S. Ermon, J. Y. Zou, S. Levine, C. Finn, and T. Ma, "Mopo: Model-based offline policy optimization," *Advances in Neural Information Processing Systems*, vol. 33, pp. 14 129–14 142, 2020.

[3] P. Jenkins, M. Selander, J. S. Jenkins, A. Merrill, and K. Armstrong, "Personalized product assortment with real-time 3d perception and bayesian payoff estimation," in *Proceedings of the 30th ACM SIGKDD Conference on Knowledge Discovery and Data Mining*, 2024, pp. 5161–5171.

[4] A. Amini, W. Schwarting, A. Soleimany, and D. Rus, "Deep evidential regression," *Advances in neural information processing systems*, vol. 33, pp. 14 927–14 937, 2020.

[5] W. Liu, X. Wang, J. Owens, and Y. Li, "Energy-based out-of-distribution detection," *Advances in neural information processing systems*, vol. 33, pp. 21 464–21 475, 2020.

[6] K. Kang, A. Setlur, C. Tomlin, and S. Levine, "Deep neural networks tend to extrapolate predictably," *arXiv preprint arXiv:2310.00873*, 2023.

[7] B. Settles, "Active learning literature survey," 2009.

[8] M. Ziatdinov, "Active learning with fully bayesian neural networks for discontinuous and nonstationary data," *arXiv preprint arXiv:2405.09817*, 2024.

[9] P. Jenkins, H. Wei, J. S. Jenkins, and Z. Li, "Bayesian model-based offline reinforcement learning for product allocation," in *Proceedings of the AAAI Conference on Artificial Intelligence*, vol. 36, no. 11, 2022, pp. 12 531–12 537.

[10] V. Dheur and S. B. Taieb, "A large-scale study of probabilistic calibration in neural network regression," in *International Conference on Machine Learning*. PMLR, 2023, pp. 7813–7836.

[11] D. A. Nix and A. S. Weigend, "Estimating the mean and variance of the target probability distribution," in *Proceedings of 1994 ieee international conference on neural networks (ICNN'94)*, vol. 1. IEEE, 1994, pp. 55–60.

[12] A. Stirn, H. Wessels, M. Schertzer, L. Pereira, N. Sanjana, and D. Knowles, "Faithful heteroscedastic regression with neural networks," in *International Conference on Artificial Intelligence and Statistics*. PMLR, 2023, pp. 5593–5613.

[13] A. Immer, E. Palumbo, A. Marx, and J. Vogt, "Effective bayesian heteroscedastic regression with deep neural networks," *Advances in Neural Information Processing Systems*, vol. 36, 2024.

[14] N. Fallah, H. Gu, K. Mohammad, S. A. Seyyedsalehi, K. Nourijelyani, and M. R. Eshraghian, "Nonlinear poisson regression using neural networks: A simulation study," *Neural Computing and Applications*, vol. 18, pp. 939–943, 2009.

[15] S.-M. Xie, "A neural network extension for solving the pareto/negative binomial distribution model," *International Journal of Market Research*, vol. 64, no. 3, pp. 420–439, 2022.

[16] S. Young, P. Jenkins, L. Da, J. Dotson, and H. Wei, "Flexible heteroscedastic count regression with deep double poisson networks," *arXiv preprint arXiv:2406.09262*, 2024.

[17] C. Guo, G. Pleiss, Y. Sun, and K. Q. Weinberger, "On calibration of modern neural networks," in *International conference on machine learning*. PMLR, 2017, pp. 1321–1330.

[18] M. Minderer, J. Djolonga, R. Romijnders, F. Hubis, X. Zhai, N. Houlsby, D. Tran, and M. Lucic, "Revisiting the calibration of modern neural networks," *Advances in Neural Information Processing Systems*, vol. 34, pp. 15 682–15 694, 2021.

[19] A. Dawid, "Objective probability forecasts," *University College London, Dept. of Statistical Science. Research Report*, vol. 14, 1982.

[20] M. P. Naeini, G. Cooper, and M. Hauskrecht, "Obtaining well calibrated probabilities using bayesian binning," in *Proceedings of the AAAI conference on artificial intelligence*, vol. 29, no. 1, 2015.

[21] J. Nixon, M. W. Dusenberry, L. Zhang, G. Jerfel, and D. Tran, "Measuring calibration in deep learning." in *CVPR workshops*, vol. 2, no. 7, 2019.

[22] V. Kuleshov, N. Fenner, and S. Ermon, "Accurate uncertainties for deep learning using calibrated regression," in *International conference on machine learning*. PMLR, 2018, pp. 2796–2804.

[23] Y. Zhang, D. Zhou, S. Chen, S. Gao, and Y. Ma, "Single-image crowd counting via multi-column convolutional neural network," in *Proceedings of the IEEE conference on computer vision and pattern recognition*, 2016, pp. 589–597.

[24] D. Lian, J. Li, J. Zheng, W. Luo, and S. Gao, "Density map regression guided detection network for rgb-d crowd counting and localization," in *Proceedings of the IEEE/CVF Conference on Computer Vision and Pattern Recognition*, 2019, pp. 1821–1830.

[25] Y. Lv, Y. Duan, W. Kang, Z. Li, and F.-Y. Wang, "Traffic flow prediction with big data: A deep learning approach," *Ieee transactions on intelligent transportation systems*, vol. 16, no. 2, pp. 865–873, 2014.

[26] C. Liu, D. Q. Huynh, Y. Sun, M. Reynolds, and S. Atkinson, "A vision-based pipeline for vehicle counting, speed estimation, and classification," *IEEE Transactions on Intelligent Transportation Systems*, vol. 22, no. 12, pp. 7547–7560, 2021.

[27] S. Li, F. Chang, C. Liu, and N. Li, "Vehicle counting and traffic flow parameter estimation for dense traffic scenes," *IET Intelligent Transport Systems*, vol. 14, no. 12, pp. 1517–1523, 2020.

[28] J. You, X. Li, M. Low, D. Lobell, and S. Ermon, "Deep gaussian process for crop yield prediction based on remote sensing data," in *Proceedings of the AAAI conference on artificial intelligence*, vol. 31, no. 1, 2017.

[29] P. Jenkins, K. Armstrong, S. Nelson, S. Gotad, J. S. Jenkins, W. Wilkey, and T. Watts, "Countnet3d: A 3d computer vision approach to infer counts of occluded objects," in *Proceedings of the IEEE/CVF Winter Conference on Applications of Computer Vision*, 2023, pp. 3008–3017.

[30] M. Marsden, K. McGuinness, S. Little, C. E. Keogh, and N. E. O'Connor, "People, penguins and petri dishes: Adapting object counting models to new visual domains and object types without forgetting," in *Proceedings of the IEEE conference on computer vision and pattern recognition*, 2018, pp. 8070–8079.

[31] M. Kull and P. A. Flach, "Reliability maps: a tool to enhance probability estimates and improve classification accuracy," in *Machine Learning and Knowledge Discovery in Databases: European Conference, ECML PKDD 2014, Nancy, France, September 15-19, 2014. Proceedings, Part II 14*. Springer, 2014, pp. 18–33.

[32] E. Hüllermeier and W. Waegeman, "Aleatoric and epistemic uncertainty in machine learning: An introduction to concepts and methods," *Machine learning*, vol. 110, no. 3, pp. 457–506, 2021.

[33] J. Park and K. Muandet, "A measure-theoretic approach to kernel conditional mean embeddings," *Advances in neural information processing systems*, vol. 33, pp. 21 247–21 259, 2020.

[34] J. Błasiok, P. Gopalan, L. Hu, and P. Nakkiran, "A unifying theory of distance from calibration," in *Proceedings of the 55th Annual ACM Symposium on Theory of Computing*, 2023, pp. 1727–1740.

[35] K. Muandet, K. Fukumizu, B. Sriperumbudur, B. Schölkopf *et al.*, "Kernel mean embedding of distributions: A review and beyond," *Foundations and Trends® in Machine Learning*, vol. 10, no. 1-2, pp. 1–141, 2017.

[36] T. Salimans, I. Goodfellow, W. Zaremba, V. Cheung, A. Radford, and X. Chen, "Improved techniques for training gans," *Advances in neural information processing systems*, vol. 29, 2016.

[37] M. Heusel, H. Ramsauer, T. Unterthiner, B. Nessler, and S. Hochreiter, "Gans trained by a two time-scale update rule converge to a local nash equilibrium," *Advances in neural information processing systems*, vol. 30, 2017.

[38] A. Radford, J. W. Kim, C. Hallacy, A. Ramesh, G. Goh, S. Agarwal, G. Sastry, A. Askell, P. Mishkin, J. Clark, G. Krueger, and I. Sutskever, "Learning transferable visual models from natural language supervision," 2021. [Online]. Available: https://arxiv.org/abs/2103.00020

[39] G. Ilharco, M. Wortsman, R. Wightman, C. Gordon, N. Carlini, R. Taori, A. Dave, V. Shankar, H. Namkoong, J. Miller, H. Hajishirzi, A. Farhadi, and L. Schmidt, "Openclip," Jul. 2021, if you use this software, please cite it as below. [Online]. Available: https://doi.org/10.5281/zenodo.5143773

[40] M. Bińkowski, D. J. Sutherland, M. Arbel, and A. Gretton, "Demystifying mmd gans," 2021. [Online]. Available: https://arxiv.org/abs/1801.01401

[41] M. Seitzer, A. Tavakoli, D. Antic, and G. Martius, "On the pitfalls of heteroscedastic uncertainty estimation with probabilistic neural networks," *arXiv preprint arXiv:2203.09168*, 2022.

[42] H. Zhang, C. Moustapha, Y. N. Dauphin, and D. Lopez-Paz, "mixup: Beyond empirical risk minimization," *International Conference on Learning Representations*, 2018. [Online]. Available: https://openreview.net/forum?id=r1Ddp1-Rb

[43] T. Gneiting and A. E. Raftery, "Strictly proper scoring rules, prediction, and estimation," *Journal of the American statistical Association*, vol. 102, no. 477, pp. 359–378, 2007.

[44] T.-Y. Lin, M. Maire, S. Belongie, J. Hays, P. Perona, D. Ramanan, P. Dollár, and C. L. Zitnick, "Microsoft coco: Common objects in context," in *Computer Vision–ECCV 2014: 13th European Conference, Zurich, Switzerland, September 6-12, 2014, Proceedings, Part V 13*. Springer, 2014, pp. 740–755.

[45] B. Wu, C. Xu, X. Dai, A. Wan, P. Zhang, Z. Yan, M. Tomizuka, J. Gonzalez, K. Keutzer, and P. Vajda, "Visual transformers: Token-based image representation and processing for computer vision," 2020.

[46] G. Panis and A. Lanitis, "An overview of research activities in facial age estimation using the fg-net aging database," in *Computer Vision-ECCV 2014 Workshops: Zurich, Switzerland, September 6-7 and 12, 2014, Proceedings, Part II 13*. Springer, 2015, pp. 737–750.

[47] J. Cheng, Y. Li, J. Wang, L. Yu, and S. Wang, "Exploiting effective facial patches for robust gender recognition," *Tsinghua Science and Technology*, vol. 24, no. 3, pp. 333–345, 2019.

[48] C. Kang, G. Valenzise, and F. Dufaux, "Eva: An explainable visual aesthetics dataset," in *Joint workshop on aesthetic and technical quality assessment of multimedia and media analytics for societal trends*, 2020, pp. 5–13.

[49] K. Kärkkäinen and J. Joo, "Fairface: Face attribute dataset for balanced race, gender, and age," *arXiv preprint arXiv:1908.04913*, 2019.

[50] I. Loshchilov and F. Hutter, "Decoupled weight decay regularization," *arXiv preprint arXiv:1711.05101*, 2017.

[51] ——, "Sgdr: Stochastic gradient descent with warm restarts," *arXiv preprint arXiv:1608.03983*, 2016.

[52] E. D. Cubuk, B. Zoph, D. Mane, V. Vasudevan, and Q. V. Le, "Autoaugment: Learning augmentation policies from data," *arXiv preprint arXiv:1805.09501*, 2018.

[53] A. Howard, M. Sandler, G. Chu, L.-C. Chen, B. Chen, M. Tan, W. Wang, Y. Zhu, R. Pang, V. Vasudevan *et al.*, "Searching for mobilenetv3," in *Proceedings of the IEEE/CVF international conference on computer vision*, 2019, pp. 1314–1324.

[54] J. Deng, W. Dong, R. Socher, L.-J. Li, K. Li, and L. Fei-Fei, "Imagenet: A large-scale hierarchical image database," in *2009 IEEE conference on computer vision and pattern recognition*. Ieee, 2009, pp. 248–255.

[55] K. Fukushima, "Visual feature extraction by a multilayered network of analog threshold elements," *IEEE Transactions on Systems Science and Cybernetics*, vol. 5, no. 4, pp. 322–333, 1969.

[56] K. Hendrickx, L. Perini, D. V. der Plas, W. Meert, and J. Davis, "Machine learning with a reject option: A survey," 2024. [Online]. Available: https://arxiv.org/abs/2107.11277

[57] B. Efron, "Double exponential families and their use in generalized linear regression," *Journal of the American Statistical Association*, vol. 81, no. 395, pp. 709–721, 1986.

[58] L. Van der Maaten and G. Hinton, "Visualizing data using t-sne." *Journal of machine learning research*, vol. 9, no. 11, 2008.

A SUPPLEMENTARY EXPERIMENTAL DETAILS

A.1 Derivation of the Marginal Distribution of Y in Figure 1

Suppose $Y|X \sim \mathcal{N}(\alpha X, 1)$, where $X \sim \mathcal{N}(0, 1)$. By normal-normal conjugacy, we know that $Y \sim \mathcal{N}(\mu_Y, \sigma_Y^2)$. We solve for μ_Y and σ_Y^2 as follows:

$$
\begin{aligned}
\mu_Y &= \mathbb{E}\left[Y\right] & \sigma_Y^2 &= \mathrm{Var}(Y) \\
&= \int_{-\infty}^{\infty} \mathbb{E}\left[Y|X\right] P(X = x) dx & &= \mathbb{E}\left[\mathrm{Var}(Y|X)\right] + \mathrm{Var}(\mathbb{E}\left[Y|X\right]) \\
&= \int_{-\infty}^{\infty} \alpha x P(X = x) dx & &= \mathbb{E}\left[1\right] + \mathrm{Var}(\alpha X) \\
&= \alpha \int_{-\infty}^{\infty} x P(X = x) dx & &= 1 + \alpha^2 \mathrm{Var}(X) \\
&= \alpha \mathbb{E}\left[X\right] & &= 1 + \alpha^2 \\
&= 0
\end{aligned}
$$

Thus, $Y \sim \mathcal{N}(0, 1 + \alpha^2)$.

A.2 Detailed Description of Experiments

In all experiments, the model that achieved the best loss on the validation set during training was selected for evaluation. This helped mitigate the overfitting that we observed with respect to NLL as training continued.

Data was split into train/val/test using a fixed random seed, allocating 70% to train, 10% to val, and 20% to test.

The AdamW optimizer [50] was used for all training jobs, with an initial learning rate of 10^{-3} that decayed to 0 on a cosine annealing schedule [51]. We used a weight decay value of 10^{-5}. For image regression tasks, we applied the standard ImageNet normalization constants and augmented with the `AutoAugment` [52] transformation during training. Though we specify the feature encoder used for each dataset, we refer the reader to our source code [3] as well as the original literature on each model to find exact details about the regression heads fit on top of each encoder.

The following subsections contain further details for the models we trained, organized by dataset. We also provide relevant licensing information and URLs for each dataset where applicable.

A.2.1 Synthetic Dataset

Following [16], the MLPs we trained for the synthetic dataset in 4.1 had layers of widths `[128, 128, 128, 64]`. Training ran for 200 epochs on a 2021 MacBook Pro CPU, with a batch size of 32.

We generated this dataset locally using the process defined by [16].

A.2.2 `FG-Net`, `AAF`, and `EVA`

We used a MobileNetV3 [53] as our feature encoder (fine-tuned from the ImageNet [54] checkpoint) for the `FG-Net`, `AAF`, and `EVA` datasets. Each feature encoder was topped by the corresponding regression head for each type of model. An effective batch size of 32 was used to train all models on each of these datasets. Training was performed in BFloat16 Mixed Precision for 200 epochs on `AAF` and `EVA`, and for 100 epochs on `FG-Net`. Training code ran on an internal cluster of 4 NVIDIA GeForce RTX 2080 Ti GPUs. Evaluation was performed on a CPU.

No licensing information is available for `FG-Net`, but it can be publicly accessed at `http://yanweifu.github.io/FG_NET_data/FGNET.zip`. AAF is hosted at `https://github.com/`

---

[3] `https://anonymous.4open.science/r/probcal-8294`

A.2.3 `COCO-People`

On `COCO-People`, we use the pooled output from a ViT backbone (initialized from the `vit-base-patch16-224-in21k` checkpoint [45, 54]), followed by a `[384, 256]` MLP with ReLU activations [55] for our feature encoder. This matches the setup used by [16]. Models were trained on an internal cluster of 2 NVIDIA GeForce RTX 4090 GPUs with an effective batch size of 256. Training ran for 30 epochs with BFloat16 Mixed Precision. All CCE evaluation was done on a single GPU of this cluster, which has 24GB of VRAM.

The `COCO` dataset from which [16] defines `COCO-People` is distributed with a CCBY 4.0 license. See `https://cocodataset.org/#home`.

B COMPUTING CCE — PRACTICAL CONSIDERATIONS

B.1 Algorithm to Compute CCE for a Model

Assuming an existing implementation of the MCMD (which can be easily derived from Equation 2 after a choice of kernel), we employ Algorithm 1 to compute CCE values for a given model f, embedder φ, and set of g.t. samples $\mathcal{S} = (x_i, y_i)_{i=1}^n$.

Algorithm 1: Procedure to estimate the conditional congruence of a model f using the CCE.

```
S ← [(φ(xᵢ), yᵢ)]ⁿᵢ₌₁ ;
S_prime ← [] ;
cce_vals ← [] ;
for i = 1 to n do
    for k = 1 to ℓ do
        Draw yᵢₖ ~ f(xᵢ) ;
        S_prime.append((φ(xᵢ), yᵢₖ)) ;
    end
end
for x in {xᵢ}ⁿᵢ₌₁ do
    cce ← MCMD(S, S_prime, φ(x)) ;
    cce_vals.append(cce) ;
end
return cce_vals, mean(cce_vals) ;
```

For an implementation of this algorithm in Python, we refer the reader to our source code.

B.2 Accelerating the CCE Computation

Though we use loops for clarity in specifying Algorithm B.1, in practice, we vectorize all computations (including measuring the MCMD across a grid of values) to decrease runtime. In addition to this vectorization, we observe significant speed-ups (on the order of 15-20×) when moving all matrix operations to a GPU.

The CCE computation can be accelerated even further (and made more numerically stable) by taking advantage of the structure of the Gram matrices involved in the MCMD (see Equation 2). Since $(\mathbf{K}_X + n\lambda\mathbf{I}_n)$ and $(\mathbf{K}_Y + m\lambda'\mathbf{I}_m)$ are positive definite and symmetric, we compute their inverses via the Cholesky decomposition (which has half the cost of the typical LU decomposition performed by linear algebra libraries). Our provided code elegantly handles these details, yielding a performant and scalable CCE implementation.
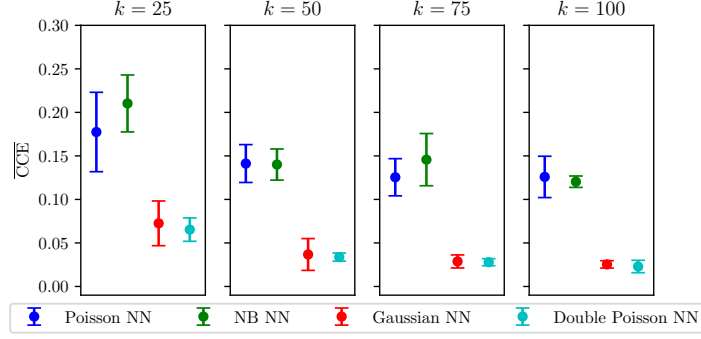
Figure 6: $\overline{\text{CCE}}$ results with various sample sizes $k < n$ ($n = 100$). The mean across 5 trials is indicated with a dot, while the error bars indicate ± 1 standard deviation.

B.3 Addressing Memory Limitations

As is common with kernel methods, the CCE (which relies on computing the MCMD for a collection of encoded inputs) grows rapidly in terms of memory requirements with the size of the data, exhibiting quadratic spatial complexity. In this work, we found that our hardware was sufficient to compute CCE values for evaluation datasets with up to $\approx 12{,}000$ examples (which requires, at peak usage, around 10 GB of memory). However, for datasets with significantly larger test splits, modifications to our technique have to be made. One approach to solve this problem is uniform downsampling: select some $k < n$, then from the test set, uniformly sample k input/output pairs. In the notation of Section 3.1.1, if $\mathcal{S} = (x_i, y_i)_{i=1}^n$ is our original sample of test data, then we downsample to obtain $\mathcal{S}_k = (x_j, y_j)_{j=1}^k$.

The risk of downsampling (as with other forms of compression) is that important signal contained in the similarities derived from the full sample, $\mathcal{S}$, can be lost from $\mathcal{S}_k$. To investigate this concern, with variously-sized uniform samples from the full test set, we compute $\overline{\text{CCE}}$ 5 times for each model trained on the synthetic data presented in Section 4.1. The results are plotted in Figure 6. Encouragingly, the relative ranking of models stays largely unperturbed, even when working with 25% of the full dataset — the Poisson and Negative Binomial models exhibit poor probabilistic fit, while the Gaussian and Double Poisson models nearly reach exact conditional congruence. The relative variance in the $\overline{\text{CCE}}$ estimator grows generally smaller as the sample size increases, which aligns with common estimation theory.

C ADDITIONAL EXPERIMENTS

C.1 Using CCE for Machine Learning with Rejection

The rising subfield of "Machine Learning with a Reject Option" centers around uncovering principled techniques for avoiding predictions when they are expected to be inaccurate or probabilistically misaligned [56]. A typical setup defines some "unreliability score" that we can compute on an arbitrary test input. We then select a threshold, and for any input with an unreliability score above that threshold, we withhold from making a prediction.

We investigate whether the CCE can be used as an effective reliability score. To do this, we train a Gaussian NN on data drawn from $X \sim \texttt{Uniform}(0, 2\pi), Y|X \sim \mathcal{N}(X \cos^2 X - \sqrt{|X| + 3}, \frac{2|2-X|+1}{8})$. As in Section 4.3, we then compute the CCE over the test split of the data without its labels (the validation split is used as $\mathcal{S}$). This simulates reality, where test labels are not available to help make decisions.

Once we have obtained CCE values, we form an increasing, nonnegative grid of thresholds $\{\tau_i\}_{i=1}^t, 0 \leq \tau_0 \leq \tau_1 \leq ... \leq \tau_t$. For each threshold τ_i, we filter our test samples to only those which incur an CCE value less than or equal to τ_i and evaluate the model's mean absolute error (MAE) and NLL on that subset. We calculate the proportion of data that was "held out" and plot
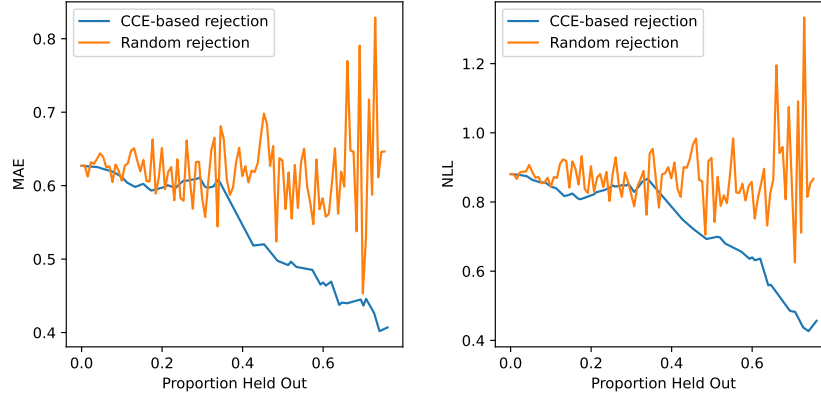
Figure 7: Results of experiment with "reject" option using CCE thresholds. The left subplot depicts how test MAE changes on the subset selected via this method, while the right depicts how test NLL changes. CCE provides a valuable mechanism for determining inputs on which predictions will be unreliable.

this proportion against each error metric. For the sake of comparison, we also compute error metrics when holding out varying proportions of data through uniform random sampling. Results are pictured in Figure 7.

C.2 Understanding the Behavior of MCMD on Known Distributions

To build intuition about the behavior of the MCMD (and illustrate why we use it as the backbone of our CCE metric), we show how it estimates distance in a variety of settings where the data generating distribution is known. We simulate two data-generating processes, one heteroscedastic, one homoscedastic. For each, we sample 1000 (x, y) pairs to represent the ground truth. We then draw 500 (x', y') pairs from 1) the same distribution; 2) a distribution with the same mean but smaller variance; 3) a distribution with the same mean but higher variance; 4) a distribution with a different mean and smaller variance; 5) a distribution with a different mean and higher variance; and 6) a distribution with an entirely different conditional relationship. Pairing each of (1-6) with the original distribution, we compute and plot the MCMD ($\sqrt{\widehat{\text{MCMD}^2}}$) between (x, y) and (x', y') across a uniform grid spanning the input space as in [33]. In addition to the MCMD plot, we report the mean value of the MCMD. We compute the MCMD with the regularization parameter $\lambda = 0.1$. To measure similarity in both x and y, we employ the RBF kernel $k_\gamma(\mathbf{x}, \mathbf{x}') = \exp\left(-\gamma||\mathbf{x} - \mathbf{x}'||^2\right)$, with $\gamma = 1$ for $k_\mathcal{X}$, and $k_\mathcal{Y}$ selected as described in Section 3.2. Results are visualized in Figures 8 and 9.

Overall, the MCMD appears to behave quite intuitively, with higher values consistently corresponding to areas where the distributions vary from each other more in both mean and standard deviation. Beyond the "eye test", we specifically highlight a few key desirable characteristics of this metric. First, we see from columns 4 and 5 of Figures 8 and 9 that poor mean fit is penalized more harshly by MCMD when the corresponding variance is low. This indicates that the MCMD requires high variance to explain misalignment of means, which is arguably the correct stipulation to enforce. Additionally, from columns 2 and 3, we observe that the MCMD recognizes the case where the means match but the spread of two distributions is different. This suggests the MCMD is robust at identifying various forms of potential discrepancy between a predictive distribution and the ground truth.

C.3 Hyperparameter Study

Computing the CCE for a given model requires a handful of up-front decisions — primarily, which functions to use for $k_\mathcal{X}$ and $k_\mathcal{Y}$ (including kernel hyperparameters) and what values to select for λ and λ'. Additionally, one must decide how many Monte Carlo samples, ℓ, to take when forming $\mathcal{S}'$ from a model f. In Section 3.2, we provide a variety of "default" settings that have proven effective in our work. To further investigate the impact of the choice of kernel, λ, and ℓ, we explore the empirical
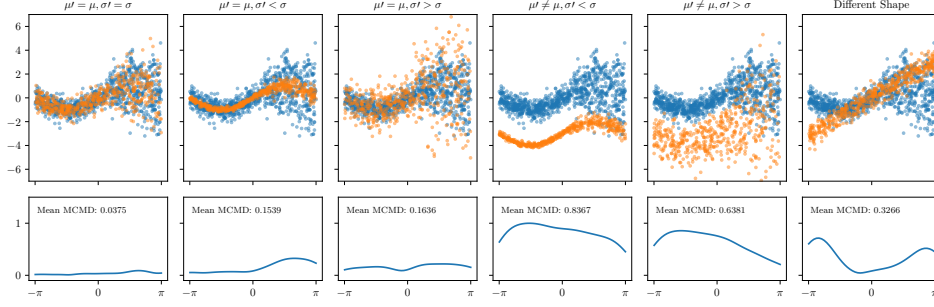
Figure 8: MCMD plots for heteroscedastic ground-truth data compared against various conditional distributions. The ground-truth mean and standard deviation are denoted μ and σ, while μ' and σ' describe the comparison sample.
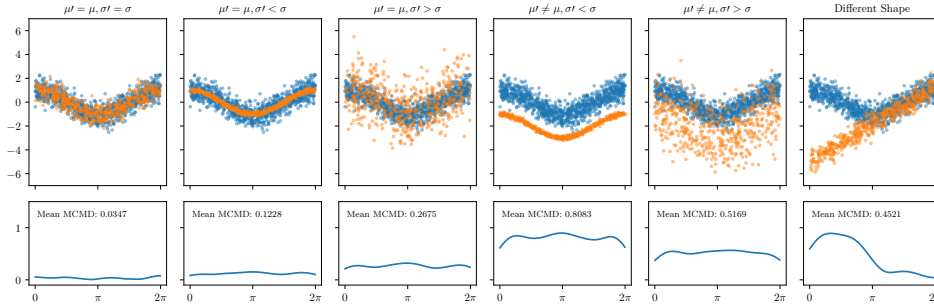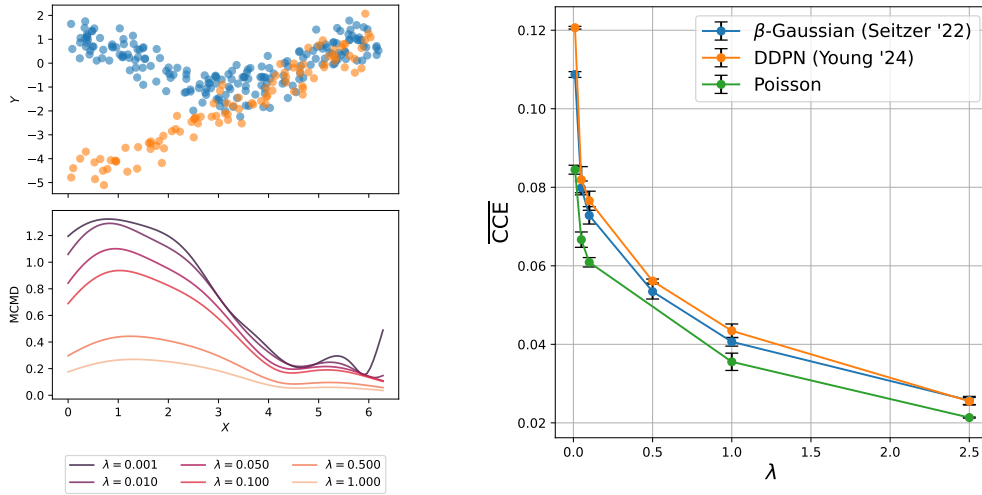

Figure 9: MCMD plots for homoscedastic data compared against various conditional distributions.

(a) The effect of λ on MCMD computations over synthetic data.

(b) The effect of λ on $\overline{\text{CCE}}$ for three models trained on COCO-People.

Figure 10: Studying the impact of the regularizer λ.

impact of these hyperparameters. To facilitate our study, we compare samples from two data-generating distributions via MCMD: (X, Y), where $X \sim \text{Uniform}(0, 2\pi)$, $Y|X \sim \mathcal{N}(\cos(X), \frac{1}{4})$ and (X', Y'), where $X' \sim \text{Uniform}(0, 2\pi)$, $Y'|X' \sim \mathcal{N}(X' - 5, \frac{1}{4})$. We also run a series of CCE computations (with differing hyperparameters) for models trained on COCO-People.

18

C.3.1 Investigating λ

To isolate the impact of λ, we first focus on how it affects the MCMD computation between our samples from (X, Y) and (X', Y') as specified above. We fix our kernels $k_{\mathcal{X}}$ (RBF kernel with $\gamma = 0.5$) and $k_{\mathcal{Y}}$ (RBF kernel with $\gamma = \frac{1}{2\sigma_Y^2}$).

We vary λ along a grid of values between 0 and 1, then compute the MCMD across the input space. For simplicity, we set $\lambda' = \lambda$. In Figure 10a we plot these MCMD values (second row), along with a scatterplot of the samples being compared (first row). Note that when λ is very small, the MCMD becomes quite sensitive to individual points (observe, for example, the spike in MCMD around 2π for $\lambda = 0.001$). As λ increases, the MCMD between the two samples grows smoother and tends toward zero. This behavior agrees with [33]'s categorization of λ as a regularizer (λ controls the regularization term in the empirical loss [33] minimize to obtain their estimate of MCMD). Thus, we can consider λ as a knob that we can turn depending on how much we "believe" that the samples represent the underlying conditional distributions being compared. When λ is large, we discard all evidence from our sample that the distributions are

Figure 11: The effect of the number of Monte Carlo samples, ℓ, on $\overline{\text{CCE}}$ for three models trained on `AAF`.

different (thus, the MCMD is 0). When λ is small, we place more weight on the individual deviations observed between samples. Generally, λ values around 0.05 or 0.1 exhibit reasonable behavior. We set $\lambda = 0.1$ in our experiments in the main body of the paper.
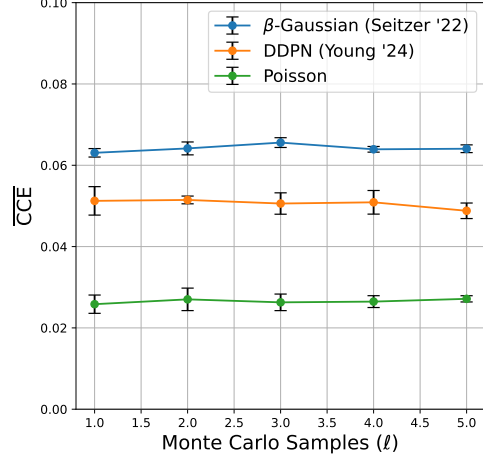
We also investigate the effect of λ on CCE (which calculates MCMD using samples obtained from a model) for three neural networks trained on the `COCO-People` dataset. Using the same regressors discussed in Section 4.2.1, we compute $\overline{\text{CCE}}$ across a grid of λ values for each model and display the results in Figure 10b. We observe a similar pattern as before: increasing λ shrinks the mean CCE values towards zero, and we aggressively discard evidence from the data. Interestingly, the relative ordering of the three models is generally preserved across the domain of λ, suggesting that using CCE to make comparisons *across* models is fairly robust to the choice of λ.

C.3.2 Modifying $k_{\mathcal{X}}$ and $k_{\mathcal{Y}}$

We next investigate the impact of the γ hyperparameter in $k_{\mathcal{X}}$ and $k_{\mathcal{Y}}$, which is present in both the RBF and Laplacian kernels. Specifically, we fix $\lambda = 0.1$ and vary γ simultaneously in $k_{\mathcal{X}}$ and $k_{\mathcal{Y}}$. We perform this experiment on the synthetic samples from (X, Y) and (X', Y') we generated earlier. We use the RBF kernel, but since γ induces a similar effect on the Laplacian kernel, we expect an equivalent analysis. Figure 12a displays how MCMD computations are affected as γ increases. Since the RBF kernel essentially computes similarities by centering a Gaussian at each point with standard deviation $\frac{1}{\sqrt{2\gamma}}$, we translate each γ value into an "ellipse of influence" spanning two standard deviations in both the x and y direction. These are visualized in light red around each point in the dataset. As γ increases, the number of points that are considered similar to a given (x, y) pair decreases (since the implied Gaussian becomes more concentrated). This increases the sensitivity of the MCMD computation, similarly to selecting low values of λ. Though most practical applications of MCMD (such as our CCE computation) will not use the RBF kernel for the input values, this behavior provides a good intuition for selecting γ for $k_{\mathcal{Y}}$. A workable heuristic is to select $\gamma = \frac{1}{2\sigma_Y^2}$, which ensures that the majority of similarities in $\mathcal{Y}$ are nonzero, with closer points exerting more influence.

Lastly, we directly compare MCMD values obtained with three different kernels: RBF, Laplacian, and Polynomial (applying the same kernel class to the input and the output spaces). For the RBF

19
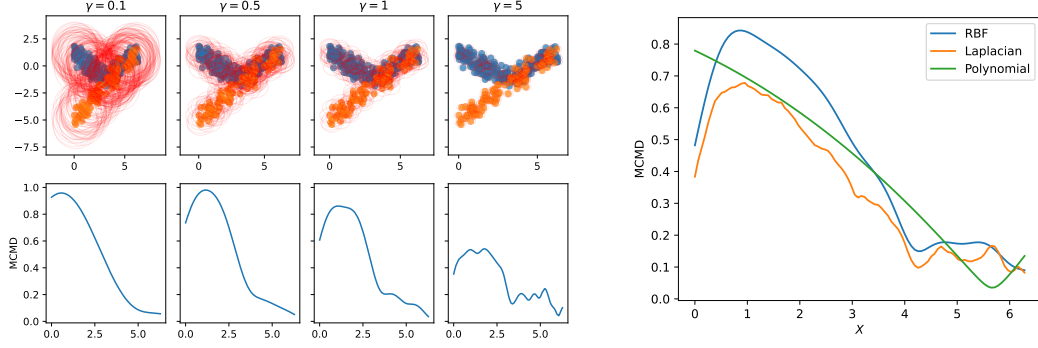
(a) The effect of the kernel hyperparameter γ. Red ellipses indicate the region around each point where similarity (as implied by the RBF kernel) is meaningfully greater than zero.

(b) The effect of the choice of kernel on the MCMD computation.

Figure 12: Studying the impact of the kernel functions $k_{\mathcal{X}}$ and $k_{\mathcal{Y}}$ on the MCMD.

and Laplacian kernels, we set $\gamma = 2$ for $k_{\mathcal{X}}$ and $\gamma = \frac{1}{2\hat{\sigma}_Y^2}$ for $k_{\mathcal{Y}}$. For the polynomial kernel, we use a degree of 3, offset of 1, and multiply the inner product by 0.02 (mostly to ensure MCMD values live on the same scale). For all MCMD computations, we set $\lambda = 0.1$. Figure 12b displays how the MCMD differs across $\mathcal{X}$ for each kernel. We note that each method largely agrees as to the regions with the most and least discrepancy between the samples. Interestingly, the polynomial kernel produces the smoothest MCMD curve, followed by RBF and Laplacian. From these results, we suspect that the choice of kernel does not matter as much as the hyperparameters associated with that kernel.

C.3.3 Increasing the Value of ℓ

Finally, we examine the impact of the number of Monte Carlo samples, ℓ, on $\overline{\text{CCE}}$ in Figure 11. Specifically, we examine the same three models from Section 4.2.1 and their performance on the AAF dataset. For each model we vary the number of samples, $\ell \in \{1, 2, 3, 4, 5\}$. We compute $\overline{\text{CCE}}$ three times and plot the mean and standard deviation over the three trials. Importantly, we observe that CCE is robust to the number of Monte Carlo samples; this effect is consistent across models. We recommend setting $\ell = 1$ to reduce computational complexity, and do so in all of our experiments.
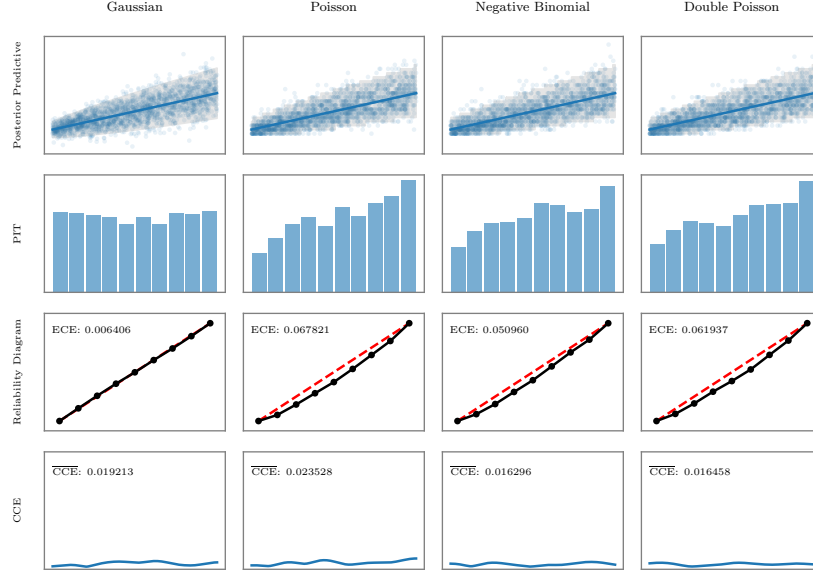
Figure 13: We simulate four data generating processes for (X, Y) with identical first and second moments. Data are drawn from a `Gaussian`, `Poisson`, `Negative Binomial`, and `Double Poisson` [57] distribution, where $X \sim \texttt{Uniform}(1, 10)$ and $Y|X$ is defined, respectively, as $\texttt{Gaussian}(X, X)$, $\texttt{Poisson}(X)$, $\texttt{NegativeBinomial}(\lceil \frac{X^2}{\varepsilon} \rceil, 1 - \varepsilon)$, where $(\varepsilon \ll 1)$, and $\texttt{Double Poisson}(X, 1)$. We draw 2000 samples from each distribution. (Row 1) A perfectly specified probabilistic model with mean and 95% centered credible intervals. (Row 2) A histogram of each model's Probability Integral Transform (PIT). (Row 3) A reliability diagram in the style of [22], along with each model's ECE ($\alpha = 1$). (Row 4) The Conditional Congruence Error (CCE) between samples drawn from each predictive distribution and the ground truth dataset. Though the histograms, reliability diagrams, and ECE values identify the well-specified Gaussian model, they fail to capture calibration for the discrete models. Meanwhile, our proposed approach using the CCE correctly indicates that each model is (with some sampling error) perfectly congruent, and thus calibrated.
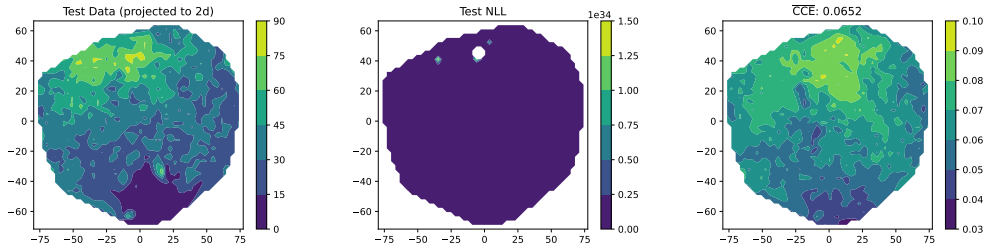

Figure 14: Comparison of NLL with CCE for pointwise analysis of probabilistic fit. From left to right: A t-SNE projection of the test split of AAF (color indicates age), the NLL values achieved by the DDPN model, and the CCE values on each test input. NLL is sensitive to outliers and is even undefined for some values (where the probability of the true target was zero). Meanwhile, CCE illuminates the input regions where the model is least congruent. In this case, these regions appear to line up with images of older faces, suggesting a potential inability of the model to reliably assess the ages of elderly people.

21

D SHORTCOMINGS OF EXISTING METRICS

D.1 On Bias in the ECE Against Discrete Models

While writing this paper, we noticed some strange behavior with [22]'s ECE score. This led us to investigate further, and we have uncovered significant issues with using this metric to quantify the calibration of discrete regression models. We first restate the definition of ECE in Equation 4:

$$\text{ECE}(F_1, y_1, ..., F_n, y_n) = \sum_{j=1}^{q} w_j \cdot |p_j - \hat{p}_j|^{\alpha} \tag{4}$$

where F_i denotes a model's predicted cumulative density function (CDF) for target y_i, we select q confidence levels $0 \leq p_1 < ... < p_q \leq 1$, and for each p_j we compute the empirical quantity

$$\hat{p}_j = \underset{i=1,...,n}{\mathbb{E}}[\mathbb{1}\{F_i(y_i) \leq p_j\}] = \frac{|\{y_i|F_i(y_i) \leq p_j, i = 1, ..., n|}{n} \tag{5}$$

This metric can be viewed as a direct application of the Probability Integral Transform (PIT; also known as universality of the uniform), since it is simply an empirical estimate of the distance (Wasserstein when $\alpha = 1$, Cramér–von Mises when $\alpha = 2$) between realizations of the PIT $Z_i = F_i(y_i)$ and $\texttt{Uniform}(0,1)$ [10].

When the assumptions of the PIT hold (namely, that $P_{Y|X=x}$ is a random variable with a continuous CDF for each x), the ECE can differentiate between well-calibrated and miscalibrated distributions. However, we note that in the discrete setting, $P_{Y|X=x}$ (and by extension, its CDF) is not continuous. In fact, a discrete CDF has a countable range, thus the PIT realizations of a discrete model can never be distributed as $\texttt{Uniform}(0,1)$. This provides reason to doubt the applicability of the ECE for count regression.

We illustrate this point empirically in Figure 13. In this figure, we simulate data from a $\texttt{Gaussian}$, $\texttt{Poisson}$, $\texttt{Negative Binomial}$, and $\texttt{Double Poisson}$ [57] distribution, each with identical mean and variance. We then perfectly specify a probabilistic model for each dataset and compute the corresponding ECE. Even though each model is known a priori to be congruent (and thus calibrated), the ECE fails to recover this fact when the data / model are discrete. Reliance on uniformity of the PIT, which is not a necessary condition for calibration in the discrete case, causes the ECE to overestimate the true calibration error for the $\texttt{Poisson}$, $\texttt{Negative Binomial}$, and $\texttt{Double Poisson}$ models (which clearly do not have uniform PITs). Meanwhile, the ECE is essentially zero for the perfectly calibrated $\texttt{Gaussian}$ model. These results support our theoretical analysis identifying the ECE as an insufficient (and biased) measure when quantifying the calibration of a discrete regression model.

D.2 On the Limited Applicability of NLL for Point-Wise Analysis

While the ECE is strictly defined in the aggregate sense, it is possible to evaluate the NLL at specific inputs (provided a label is available) to gain some understanding about point-wise probabilistic fit. In practice, however, we find that because NLL lacks context outside the specific point being evaluated, it is sensitive to outliers and produces a rather discontinuous loss surface. Additionally, since NLL has no fixed lower bound, it can be hard to interpret just how close to perfectly-fit a given predictive distribution is ([34] discusses this in some detail). These shortcomings do not extend to the CCE, as its kernelized computation incorporates similar inputs and outputs when assessing congruence and its minimum is 0. As an added bonus, the CCE can be computed on inputs that do not have a label (see Section 4.3 for an explanation of how this works).

To make a more concrete comparison between the NLL and CCE as tools for point-wise comparison, we assess the conditional distributions learned by the DDPN [16] trained on $\texttt{AAF}$ in two ways: by computing the NLL for each test point, and by computing the CCE for each test point (using the validation split as $\mathcal{S}$). We use t-SNE [58] to project the embeddings of each input $\varphi(x_i)$ to two dimensions for easy visualization, and create a contour plots indicating NLL and CCE across the input space. To build intuition around the geometric structure of the input space, we also provide a plot showing the magnitude of the labels for each test input. Results are displayed in Figure 14.

E   ADDITIONAL CASE STUDIES

E.1   `AAF`

Additional case studies in the style of Section 4.3 for the various models we trained on the `AAF` dataset can be found in Figures 15, 16, 17, 18, 19, and 20 (excepting the β-Gaussian, which is displayed in Figure 4 in the main body).

E.2   `COCO-People`

We also provide additional case studies showing the best and worst examples in terms of CCE for each model trained on the `COCO-People` dataset (excepting the Poisson that we showcase in Figure 5 in the main body). See Figures 21, 22, 23, 24, 25, and 26.
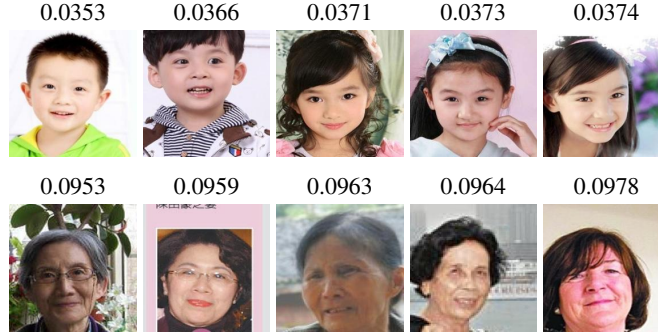

Figure 15: AAF test images that incurred the lowest (first row) and highest (second row) CCE values for the DDPN model.
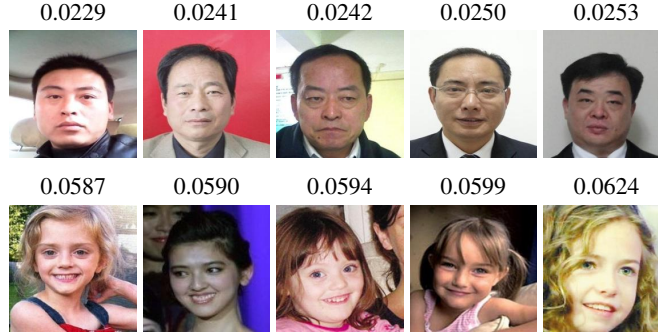

Figure 16: AAF test images that incurred the lowest (first row) and highest (second row) CCE values for [12]'s "faithful" Gaussian.
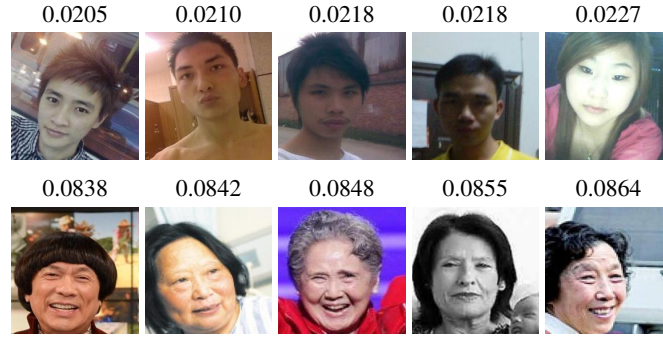
Figure 17: AAF test images that incurred the lowest (first row) and highest (second row) CCE values for a Gaussian NN.
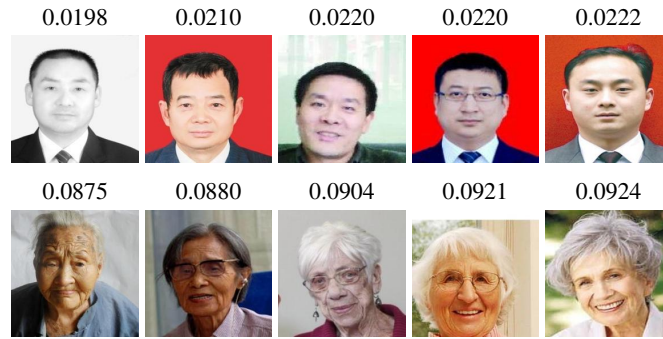

Figure 18: AAF test images that incurred the lowest (first row) and highest (second row) CCE values for [13]'s Natural Gaussian.
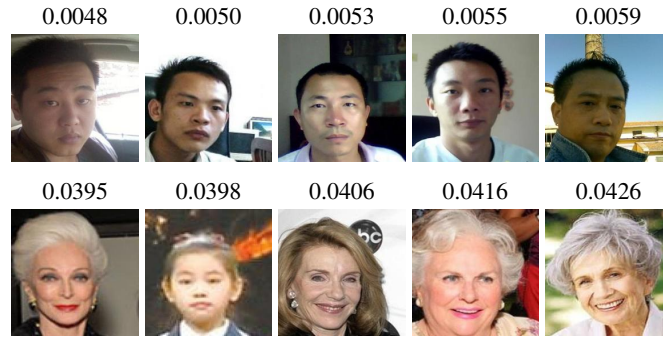

Figure 19: AAF test images that incurred the lowest (first row) and highest (second row) CCE values for a Negative Binomial NN.
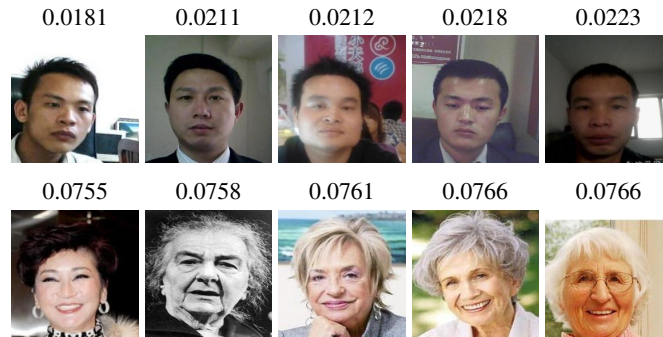
Figure 20: AAF test images that incurred the lowest (first row) and highest (second row) CCE values for a Poisson NN.

Figure 21: `COCO-People` test images that incurred the lowest (first row) and highest (second row) CCE values for the DDPN model.

Figure 22: `COCO-People` test images that incurred the lowest (first row) and highest (second row) CCE values for [12]'s "faithful" Gaussian NN.

0.0974	0.0980	0.0986	0.0990	0.0993

0.1556	0.1558	0.1567	0.1575	0.1577

Figure 23: `COCO-People` test images that incurred the lowest (first row) and highest (second row) CCE values for a Gaussian NN.

0.0576	0.0589	0.0592	0.0594	0.0600

0.1224	0.1225	0.1225	0.1226	0.1246

Figure 24: `COCO-People` test images that incurred the lowest (first row) and highest (second row) CCE values for [13]'s natural Gaussian NN.

0.0489	0.0493	0.0495	0.0500	0.0502

0.1060	0.1072	0.1080	0.1081	0.1109

Figure 25: `COCO-People` test images that incurred the lowest (first row) and highest (second row) CCE values for a Negative Binomial NN.

Figure 26: `COCO-People` test images that incurred the lowest (first row) and highest (second row) CCE values for a β-Gaussian NN [41].